World Scientific
www.worldscientific.com

Properties of the chalcogenide-based double perovskites Ba$_2$NbBiS$_6$ and Ba$_2$TaSbS$_6$ with respect to structural, electronic and optical aspects

H. Baaziz [iD]*, T. Ghellab [iD] and Z. Charifi [iD]

Department of Physics, Faculty of Science,
University of M'sila, 28000 M'sila, Algeria

Laboratory of Physics and Chemistry of Materials,
University of M'sila, M'sila, Algeria
*hakim.baaziz@univ-msila.dz

In this work, we delve into the investigation of the structural, electronic, and optical properties of Ba$_2$NbBiS$_6$ and Ba$_2$TaSbS$_6$ chalcogenide-based double perovskites, which are structured in the cubic space group $Fm\bar{3}m$ form. We have performed first-principles calculations using density functional theory (DFT) to study the above properties. The electronic band structure and density of states of this compound have been investigated, and their results show that Ba$_2$NbBiS$_6$ and Ba$_2$TaSbS$_6$ exhibit a semiconducting nature with an indirect energy gap of 1.680 eV and 1.529 eV, respectively. Furthermore, an investigation was conducted on the optical properties of the compounds throughout the energy range spanning from 0 eV to 55 eV. This investigation focused on many parameters, including dielectric functions, optical reflectivity, refractive index, extinction coefficient, optical conductivity, and electron energy loss. The optical data obtained from the calculations reveals that all compounds demonstrate isotropy in optical polarization. Furthermore, it has been noted that our compounds exhibit absorption properties inside the ultraviolet (UV) region. Consequently, these materials hold promise as potential candidates for various applications, such as UV photodetectors, UV light emitters, and power electronics. This is primarily attributed to their inherent absorption limits and the presence of prominent absorption peaks in this spectral range. In brief, chemical mutation techniques have been employed to manipulate the characteristics of double-sulfide perovskites to develop durable and environmentally friendly perovskite materials suitable for solar purposes.

Keywords: DFT; optoelectronics; chalcogenide double perovskites; optical properties.

PACS numbers: 71.20.Nr, 78.20.−e, 71.15.−m, 71.10.−w

*Corresponding author.

H. Baaziz, T. Ghellab & Z. Charifi

1. Introduction

Recent in-depth research into organic-inorganic hybrid perovskite (OIHP), $CH_3NH_3PbX_3$ (X = Cl, Br, and I), has revolutionized the field of solar cells. The laboratory-scale power conversion efficiency (PCE) has been recently revised to 23.3%,[1] surpassing the previous value of 3.8% reported in 2009.[2] The efficiency of commercially available thin-film solar cells, specifically CdTe (22.1%) and $CuIn_xGa_{1-x}Se_2$ (22.9%), is equivalent to this updated PCE. Nonetheless, the enduring stability and potential toxicity of Pb provide considerable obstacles to its extensive utilization in industrial environments. Significant endeavors have been undertaken in recent times to explore and investigate other options, to address and surmount the aforementioned challenges. The substitution of the organic $CH_3NH_3^+$ with the inorganic Cs^+ cation presents an alternative, given that the $CsPbX_3$ (X = Cl, Br, I) exhibits enhanced thermal stability and lacks volatile organic constituents. $CsPbBr_3$ exhibits good stability, but it possesses a relatively wide bandgap ranging from 2.3 eV to 2.4 eV.[3,4] On the other hand, $CsPbI_3$ possesses a more suitable bandgap of 1.73 eV. However, it is afflicted by persistent phase instability in the long term.[5,6] However, recent studies by You *et al.*[7] have demonstrated a PCE of 15.7% when the precursor film undergoes controlled growth in a dry atmosphere. Additionally, Zhao *et al.*[8] achieved a champion efficiency of 17.06% by employing PTABr post-treatment. The compound $CsPbI_2Br$ exhibited a favorable balance between its bandgap and phase stability, resulting in the development of devices that obtained rather high efficiencies. Specifically, the reported efficiencies were 13.3%,[9] 13.47%[10] and 14.45%.[11] Nevertheless, a discrepancy in PCE persists between ILHP and OHIP, amounting to 23.3%. This disparity can be attributed to the substantial bandgaps exhibited by CsPbI3 (1.73 eV) and $CsPbI_2Br$ (1.91 eV), which exceed the optimal range (1.0–1.6 eV) for effective absorption in single-junction solar cells, as stipulated by the Shockley–Queisser limit.[12] Furthermore, the issue of lead toxicity continues to be an inherent challenge for the International Lead Health Partnership (ILHP). In the inorganic cesium halide double perovskites $Cs_2M(I)$–$M(III)X_6$ (where X stands for chlorine, bromine or iodine), the toxicity of lead (Pb) is lessened by splitting the divalent Pb(II) ions in the ILHP $CsPbX_3$ (where X stands for chlorine, bromine or iodine) into single M(I) ions and three M(III) ions. Three double perovskite compounds, namely, $Cs_2AgBiBr_6$,[13,14] $Cs_2AgBiCl_6$[13,15] and $Cs_2AgSbCl_6^-$[16,17] have been successfully synthesized. These compounds belong to the $Cs_2AgM(III)X_6$ family, where M(III) represents either Sb or Bi, and X denotes Cl, Br or I. It is worth noting that these compounds possess indirect bandgaps, which can be attributed to the mismatch between Ag orbitals and Sb/Bi *s*-orbitals at the band edges.[18,19] Consequently, their suitability as absorbers for thin-film solar cells is compromised. Cs_2AgInX_6 (X = Cl, Br) was synthesized by substituting Sb/Bi with In and exhibited direct bandgaps.[16,20]

Parity-gap transitions make it so that Cs_2AgInX_6 (where X can be Cl or Br) doesn't absorb light as well as it should.[21] The authors Zhao *et al.*[22] have put up $Cs_2InBiCl_6$ and

Cs$_2$InSbCl$_6$ as potential absorbers because of their direct bandgaps and pronounced transitions between band edges. However, it should be noted that the oxidation process of In$^+$ to In^{+3} may result in their spontaneous decomposition.[23] Meng *et al.* and Zhang *et al.* conducted a comprehensive investigation of the electronic and optical characteristics of the inorganic double cesium halide perovskite class Cs$_2$M(I)M(III)X$_6$ (where X represents Cl, Br or I). Their findings indicated that, despite being derived from the organic–inorganic hybrid perovskite (OIHP) structure, this particular class displayed distinct electronic and optical properties, which consequently diminished its potential as a viable material for solar cell absorption.

To address the inherent instability of halides, researchers have lately suggested the use of chalcogenide-based perovskites as prospective absorbers in solar cells. This is due to the anticipated fourfold increase in Coulomb interaction in chalcogenides compared to halides in systems that are fully ionic. The feasibility of employing a certain group of ABX$_3$ perovskites (where A represents Ca, Sr, and Ba; B represents Ti, Zr, and Hf; and X represents S, and Se) as absorbers in solar cells was examined through theoretical analysis by Sun *et al.*[24] One of the candidates that emerged from the study was BaZrS$_3$, which was put out as a highly promising option. It was then synthesized in laboratory experiments, and the results revealed a direct bandgap ranging from 1.73 eV to 1.85 eV, as reported in Refs. 25–27. In their study, Ju *et al.*[28] examined a total of 18 distinct ABX$_3$ chalcogenide perovskites, where A represents Ca, Sr, or Ba; B represents Ge, Sn, or Te; and X represents S or Se. The authors suggested that by combining SrSnS$_3$ and SrSnSe$_3$ in specific proportions, it is possible to modulate the bandgap to achieve optimal absorption of sunlight. Regrettably, there is currently a lack of reported chalcogenide perovskite solar cells. Nevertheless, both BaZrS$_3$ and SrSn(S, Se)$_3$ do not possess single-pair *s*-orbitals, which is regarded as a critical determinant for achieving good OIHP efficiency. This study involves chemically mutating B-site cations in BaZrS$_3$, i.e., Zr(IV) → M(III) + M(V), by replacing Zr(IV) with M(III) and M(V), where M(III) = Sb^{3+} or Bi^{3+} and M(V) = Nb^{5+}, Ta^{5+}. This mutation allows for the introduction of lone-pair *s* orbitals on a B site, resulting in the formation of a group of chalcogenide double perovskites known as Ba$_2$M(III)M(V)S$_6$. Therefore, the class of chalcogenide double perovskites preserves the two important factors that contribute to the excellent performance of OIHP: the presence of lone-pair *s* elements and the perovskite-derived structures. Our study reveals that this class of compounds possesses a similar electronic structure to OIHP. Specifically, the valence band maximum (VBM) is primarily composed of antibonding states between M(III) *s* and anion *p*, while the conduction band minimum (CBM) consists of a combination of M(III) *p*-anion *p* and M(V) *d*-anion *p*, resulting in symmetric holes and electron masses. Additionally, these compounds may exhibit quasi-direct bandgaps, with indirect bandgaps only slightly lower (0.0–0.2 eV) than the direct bandgaps. This characteristic facilitates the separation of photo-excited electrons and holes. Furthermore, the optical absorption of these compounds is stronger than that of OIHP due to their higher joint density of states in the *p*-to-*d* transition.

H. Baaziz, T. Ghellab & Z. Charifi

Organic–inorganic hybrid perovskite solar cells have rapidly emerged as a new solar cell technology, with a certified PCE of 23.7%, surpassing that of conventional thin-film contenders. Nevertheless, the limited durability and harmful nature of Pb provide significant obstacles to its widespread use in the market. Recent efforts have focused on using theoretical calculations and experimental trial-and-error methods to discover alternative perovskites. These include inorganic halide perovskites such as $CsPbI_3$ and $CsPbIBr_2$, inorganic halide double perovskites like $Cs_2AgBiBr_6$, and chalcogenide single perovskites such as $BaZrS_3$. Nevertheless, hybrid perovskite outperforms them in terms of both cell performance and material toxicity. This study thoroughly examines the stability, electronic, and optical properties of a class of lead-free chalcogenide double perovskites, namely, $A_2M(III)M(V)X_6$ compounds. In these compounds, A represents Ba^{2+}, M(III) represents Bi^{3+} or Sb^{3+}, M(V) represents Nb^{5+} or Ta^{5+}, and X represents Se^{2-}. The analysis of fundamental principles, such as bandgaps, effective masses, optical absorption, and ideal power conversion efficiencies, allowed for the identification of two stable double chalcogenide perovskites. These perovskites possess exceptional optoelectronic properties, including quasi-direct bandgaps, well-balanced electron and hole effective masses, and high optical absorption. These properties are attributed to the strong antibonding nature observed at both the VBM and CBM. This study used first-principles simulations to investigate the structural, electronic, and optical properties of the recently discovered compounds Ba_2NbBiS_6 and Ba_2TaSbS_6. The methodology for doing calculations is described in Sec. 2 of this study, while Sec. 3 is devoted to the analysis and interpretation of the results. Section 4 functions as the climax of the preceding discourse, providing the ultimate outcomes and deductions.

2. Details of Calculation

We employed the full-potential linearized augmented plane wave (FPLAPW) method of density functional theory (DFT)[29] and the Vienna package (WIEN2k)[30] to investigate the structural, electronic, and optical characteristics of the double perovskites Ba_2NbBiS_6 and Ba_2TaSbS_6. To determine the exchange-correlation potential, we employed the local density approximation (LDA)[31] and the Perdew, Burke, and Ernzerhof-based generalized gradient approximation (PBE–GGA).[29] The plane wave expansion was truncated at an energy cut-off of 400 Ryd, and the relaxation of the relative atomic positions was terminated once the energy level reached 10^{-4} Ryd. The computations were conducted with self-consistency, adhering to charge and atomic force convergence criteria of 0.001 e and 0.05 mRy/a.u, respectively. The assessment of convergence concerning the basis size relies on evaluating the product of the lowest radius of the muffin-tin sphere and the maximum vector of the plane wave, denoted as $R_{MT}^{min} \times K_{MAX} = 9$. The calculation of structural and electronic properties required the use of 1000 k-points, while a denser set of 20,000 k-points was needed for the calculation of optical properties. The research used a plane wave cut-off of $G_{max} = 12$ $(a.u.)^{-1}$ and examined R.M.T. values ranging

from 1.94 a.u. to 2.5 a.u. for the elements Ba, Nb, Bi, Ta, Sb and S. To ascertain the parameter of the equilibrium lattice and investigate the relationship between the total energy and this parameter, we conducted structural optimizations on the double perovskite compounds Ba_2NbBiS_6 and Ba_2TaSbS_6. We performed a self-consistent computation of the total energy using the WIEN2k code for several values of the lattice parameter a, which were chosen close to the experimental value. To ascertain the equilibrium parameters, including the lattice parameter (a), the compressibility modulus B, and its derivative B', the total energy was computed as a function of volume. The resulting curve was subsequently interpolated using the Murnaghan equation of state,[32] which is provided as

$$E(V) = E_0 + \frac{B}{B'(B'+1)} \left[V \left(\frac{V_0}{V} \right)^{B'} - V_0 \right] + \frac{B}{B'} (V - V_0), \qquad (1)$$

where E_0, B, and V_0 are, respectively, total energy, compressibility modulus, and equilibrium volume. The equilibrium volume is given by the minimum of the curve $E(V)$. The compressibility modulus is determined at the minimum of the $E(V)$ curve by the relation:

$$B = V \frac{\partial^2 E}{\partial V^2}. \qquad (2)$$

B': The derivative of the compressibility modulus:

$$B' = \frac{\partial B}{\partial P}. \qquad (3)$$

The electronic and optical properties were measured using the modified Becke–Johnson (mBJ) semi-local exchange potential,[33] which is thought to be the most accurate method available at the moment. It has been observed that the mBJ functional yields a more precise estimation of the bandgap when compared to the commonly employed LDA/GGA functionals.[34–38] The potential being evaluated is independent of orbitals and can accurately predict the bandgap of various materials, such as insulators, semiconductors, and transition metal oxides. This prediction shows a high level of correlation.[39–42]

3. Results and Discussion

3.1. *Structural description*

The perovskite ABX_3 exhibits a cubic structure characterized by high symmetry $Pm\bar{3}m$, wherein a single type of octahedron is present, as depicted in Fig. 1(a). The crystal structure of the double-cubic perovskite $A_2B^1B^2X_6$ is classified under a specific space group $Fm\bar{3}m$. It can be conceptualized as an ABX_3 structure, where the B site is substituted with B^1 and B^2. This substitution results in the presence of two distinct types of octahedra arranged in an alternating manner within a CFC rock-salt structure, as depicted in Fig. 1(d). From a geometric perspective, it can be observed
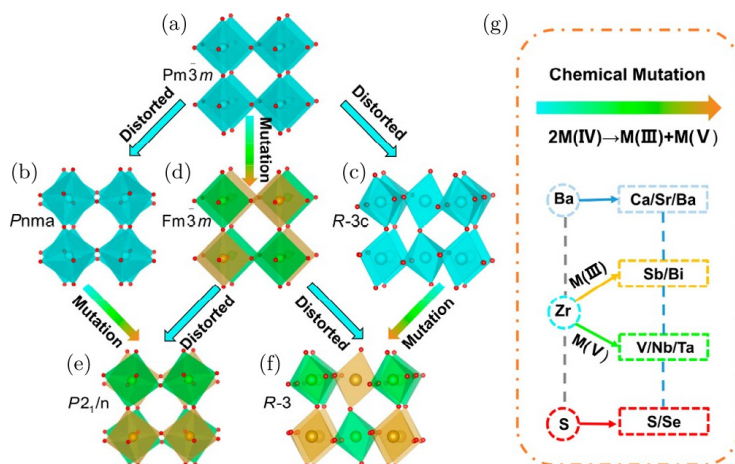
Fig. 1. (Color online) The schematic representations structures of crystals: (a) cubic perovskite (symmetry $Pm\bar{3}m$), deformed perovskite (b) ($Pnma$), (c) ($R\bar{3}c$), (d) double perovskite ($Fm\bar{3}m$), deformed double perovskite, (e) ($P2_1/n$) and (f) ($R\bar{3}$). The chemical mutation of 36 varieties of double chalcogenide perovskites (S, Se) derived from BaZrS$_3$ is depicted in the right-hand panel (g).

that in a perfect cubic perovskite, the A–X bond length is equivalent to the $\sqrt{2}*$ length of the B–X bond. The latter is commonly approximated as the sum of the ionic radii of the atoms involved. In practice, it is uncommon for ionic radii to exhibit full congruence, and the disparity between the sizes of cations and anions is frequently quantified using the Goldschmidt tolerance factor $t = \frac{(r_A + r_X)}{\sqrt{2}(r_B + r_X)}$, the ionic radii of the A, B, and X ions are denoted as r_A, r_B and r_X, respectively. Typically, solids with a tolerance factor ranging from 0.9 to 1.0 possess an optimal cubic structure, while those with a tolerance factor ranging from 0.71 to 0.9 have a deformed perovskite structure characterized by tilted octahedra. Nonperovskite structures are frequently observed to occur when the tolerance factor exceeds 1 or falls below 0.71.[43] Based on these empirical guidelines, it has been observed that a total of 36 chalcogenide compounds, characterized by the chemical formula A$_2$M(III)M(V)X$_6$ (where X represents either sulfur or selenium), have the potential to adopt distorted perovskite structures. This structural transformation is contingent upon the tolerance factors falling within the range of 0.75–0.91. There exist a total of 15 distinct perovskite phases that are characterized by their separate symmetries. Vasala's statistical analysis has revealed that in double oxide perovskites, four distinct phases are dominant. These phases are identified as a^{0}a^{0}c$^-$($I4/m$), a^{0}b$^-$b$^-$($I2/m$), a$^-$a$^-$a$^-$($R\bar{3}$), and a$^-$b$^+$a$^-$($P2_1/n$) according to the Glazer notation, with their respective space group symmetries indicated in brackets.[44] The arrangements of crystals are illustrated in Fig. 1, organized in ascending order according to the tilt dimensions.

The researchers made the observation that phases exhibiting three inclinations, specifically ($P2_1/n$ and $R\bar{3}$), demonstrate greater stability when compared to phases

having two inclinations ($I2/m$) and one inclination ($I4/m$). The observation that double perovskite structures require a higher level of flexibility in the octahedral tilt can explain the aforementioned phenomenon. This is crucial to minimize the overall energy of the system through the compression of the A-site space and the subsequent augmentation of the atomic packing fraction. The crystal structure of the double perovskite A$_2$B^{1}B^{2}X$_6$, which belongs to the $P2_1/n$ ($R\bar{3}$) space group (see Figs. 1(e) and 1(f)), can be obtained from the single perovskite ABX$_3$, which belongs to the $Pnma$ ($R\bar{3}c$) space group (see Figs. 1(b) and 1(c)), through a transformation of the B atom into B^1 and B^2. This transformation is analogous to $Pm\bar{3}m$ depicted in Fig. 1 (a), transforming into $Fm\bar{3}m$ (Fig. 1(d)). In addition, it is common to observe the $P2_1/n$ and $R\bar{3}$ phases in double oxide perovskites, including Ba$_2$CoNbO$_6$, Ba$_2$CeIrO$_6$ ($P2_1/n$) and Ba$_2$BiTaO$_6$, Ba$_2$BiNbO$_6$ ($R\bar{3}$).[43] Hence, in this investigation, the optoelectronic characteristics of the chalcogenide materials Ba$_2$NbBiS$_6$ and Ba$_2$TaSbS$_6$ are examined using double-deformed perovskites possessing the space group $Fm\bar{3}m$.

The compounds Ba$_2$NbBiS$_6$ and Ba$_2$TaSbS$_6$ possess a perovskite structure that has been crystallized within the cubic space group $Fm\bar{3}m$. Barium (Ba) is chemically bound to twelve identical sulfur (S) atoms, resulting in the formation of BaS12 cuboctahedra. These cuboctahedra share their corners with twelve equivalent BaO12 cuboctahedra, their faces with six equivalent BaS12 cuboctahedra, and their faces with four equivalent (Ta/Nb)S6 octahedra and (Bi/Sb)S6 octahedra (as depicted in Fig. 2). The Ba–S bond lengths in the material Ba$_2$NbBiS$_6$ (Ba$_2$TaSbS$_6$) are measured to be 3.594 Å and 3.565 Å when using the GGA approximation, and 3.547 Å and 3.524 Å when using the LDA approximation. (Tantalum/Niobium) is chemically attached to six identical sulfur (S) atoms, resulting in the formation of (Tantalum/Niobium)O6 octahedra. These octahedra share their corners with six equivalent (Bismuth/Antimony)O6 octahedra and their faces with eight BaS12 cuboctahedra. The octahedra that share the corners do not exhibit any inclination. The bond lengths of Nb–S (Ta–S) in the combination Ba$_2$NbBiS$_6$ (Ba$_2$TaSbS$_6$) are measured to be 2400 Å and 2381 Å (2408 Å and 2376 Å) using the GGA and LDA approximations, respectively. The element (Bi/Sb) forms chemical bonds with six S atoms, resulting in the formation of (Bi/Sb)S6 octahedra. These octahedra share their corners with six (Ta/Nb)S6 octahedra and their faces with eight BaS12 cuboctahedra. The octahedra that share the corners exhibit no tilting. The compound Ba$_2$NbBiS$_6$ (Ba$_2$TaSbS$_6$) has Bi–S (Sb–S) bond lengths of 2.678 Å and 2.656 Å (2.605 Å and 2.605 Å) when calculated using the GGA and LDA approximations, respectively. The element S is coordinated in a two-coordinate geometry to four Ba$+^2$ atoms, one atom of either Ta or Nb, and one atom of either Bi or Sb (refer to Fig. 2).

In the present investigation, the compounds undergo complete relaxation for all volumes by force optimization. The atomic positions of all compounds were determined using the LDA and GGA approximations and are presented in Table 1. Figure 3 below uses both LDA and GGA approximations to depict the variations in total energy by volume of the quaternary compounds Ba$_2$NbBiS$_6$ and Ba$_2$TaSbS$_6$. Regrettably, there is a lack of experimental results that can be used for comparative
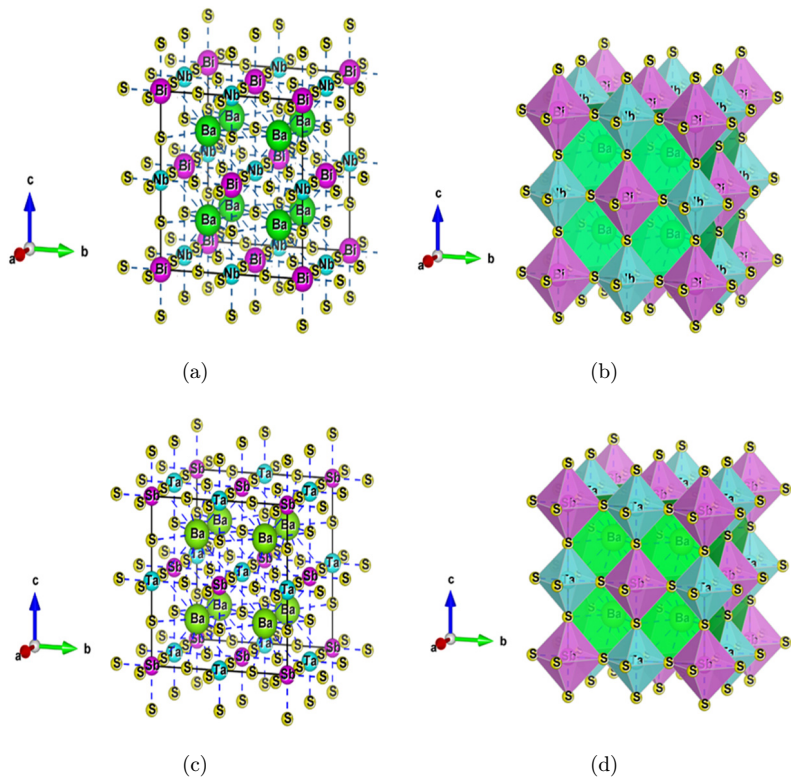
(a)

(b)

(c)

(d)

Fig. 2. (Color online) Crystal structure of the compounds Ba_2NbBiS_6, and Ba_2TaSbS_6 (a), (c) face-centered cubic (space group $Fm\overline{3}m$) along the (111) plane, and (b), (d) octahedral configuration of the groups in XS_6 (X = Ba, Nb, Ta, Sb, Bi).

analysis. The results of this study are the first to show the E_{min}, B_0, and B' ground-state energies of the quaternary chalcogenide-based double perovskite compounds Ba_2NbBiS_6 and Ba_2TaSbS_6. The results presented in Table 2 indicate that the total equilibrium energy for both compounds is significantly lower when using the GGA approximation than when using the LDA approximation. Once the Ba_2NbBiS_6

Table 1. Atomic positions of Ba_2NbBiS_6 and Ba_2TaSbS_6.

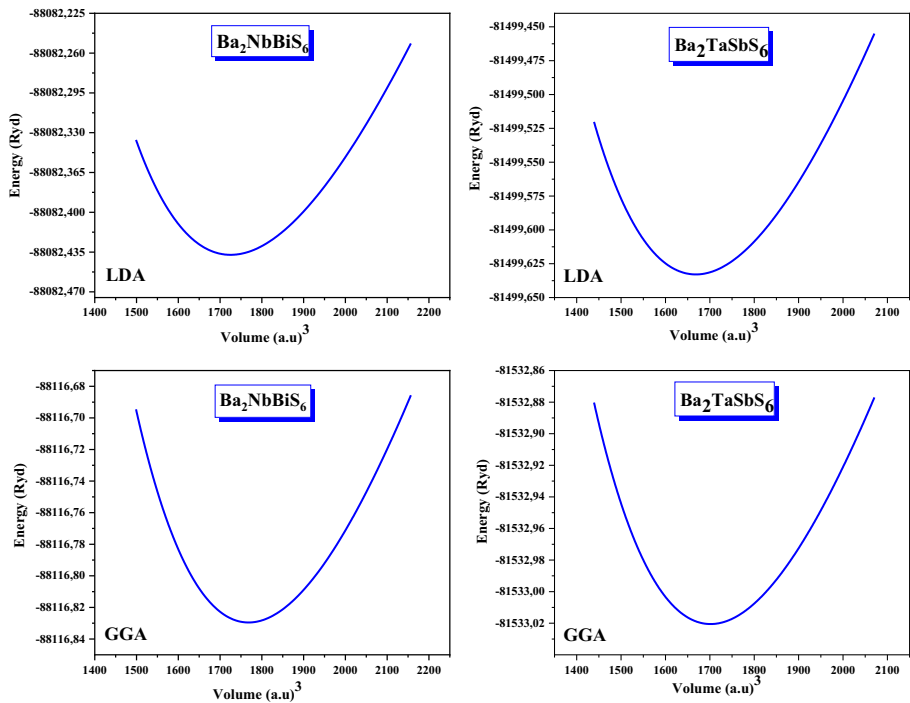| Compounds	Atomic positions	
	GGA	LDA
Ba_2NbBiS_6	Ba: (0.25, 0.25, 0.25)	Ba: (0.25, 0.25, 0.25)
	Bi: (0, 0, 0)	Bi: (0, 0, 0)
	Nb: (0.5, 0, 0)	Nb: (0.5, 0, 0)
	S: (0, 0, 0.263721)	S:(0, 0, 0.263627)
Ba_2TaSbS_6	Ba:(0.75, 0.25, 0.25)	Ba: (0.75, 0.25, 0.25)
	Sb: (0, 0, 0)	Sb:(0, 0, 0)
	Ta: (0.5, 0, 0)	Ta:(0.5, 0, 0)
	S:(0.5, 0.240178, 0)	S:(0.5, 0.238467, 0)

Fig. 3. (Color online) Variation of total energy E(Ryd) by volume for the quaternary compounds Ba_2NbBiS_6 and Ba_2TaSbS_6 with the approximations LDA and GGA.

compound is substituted with the Ba_2TaSbS_6 compound, the lattice constants (a) decrease with an increase in the compressibility modulus B. The bulk modulus for Ba_2NbBiS_6 is smaller than for the Ba_2TaSbS_6 compound, which is accompanied by a large equilibrium volume (see Table 2). Ba_2NbBiS_6 (Ba_2NbBiS_6) is found to have the

Table 2. Theoretical structural parameters using LDA and GGA of quaternary compounds of the chalcogenide-based double perovskites Ba_2Nb-BiS_6 and Ba_2TaSbS_6.

	Double chalcogenide perovskites	
Approximations	Ba_2NbBiS_6	Ba_2TaSbS_6
GGA	$a = 10.1584$ Å	$a = 10.0292$ Å
	$B_0 = 71.0646$ GPa	$B_0 = 74.8654$ GPa,
	$B' = 4.4521$	$B' = 4.3735$
	$V_0 = 1768.5154$ Boh^3	$V_0 = 1701.8902$ Boh^3
	$E_0 = -88116.829638$ Ryd	$E_0 = -81533.020613$ Ryd
LDA	$a = 10.0762$ Å	$a = 9.9641$ Å
	$B_0 = 76.2068$ GPa	$B_0 = 79.5824$ GPa
	$B' = 4.4782$	$B' = 4.3908$
	$V_0 = 1725.9331$ Boh^3	$V_0 = 1668.9703$ Boh^3
	$E_0 = -88082.437463$ Ryd	$E_0 = -81499.632969$ Ryd

2550066-9

lowest (highest) hardness compared to all the compounds examined. The Ba_2NbBiS_6 compound exhibits a soft character due to the weaker bonding interaction between Nb/ Bi and S, whereas the Ba_2NbBiS_6 compound exhibits a hard character due to the stronger bonding interaction between Ta/Sb and S. Finally, it should be noted that the lattice parameter increases with the growth of the atomic number of the Z atom in Ta/Sb atoms in Ba_2TaSbS_6 and Nb/Bi atoms in Ba_2NbBiS_6. However, the modulus of compressibility adopts the opposite behavior, it decreases when the atomic number of the Z atom increases. To date, there is no published data on the compressibility modulus values of these fascinating materials. The results obtained by calculation may facilitate the launch of empirical initiatives aimed at characterizing these innovative materials.

3.2. *Electronic properties*

The band structure of the compounds Ba_2NbBiS_6 and Ba_2TaSbS_6 exhibits a semiconducting nature, as shown in Fig. 4. The VBM and CBM are located at the L and X high symmetry points, respectively, and the Fermi energy is close to the VBM. It is very clear that the phase $Fm\bar{3}m$ is an indirect bandgap L $\rightarrow$ X for both compounds Ba_2NbBiS_6 and Ba_2TaSbS_6 using the LDA, GGA, mBJ–LDA, and mBJ–GGA
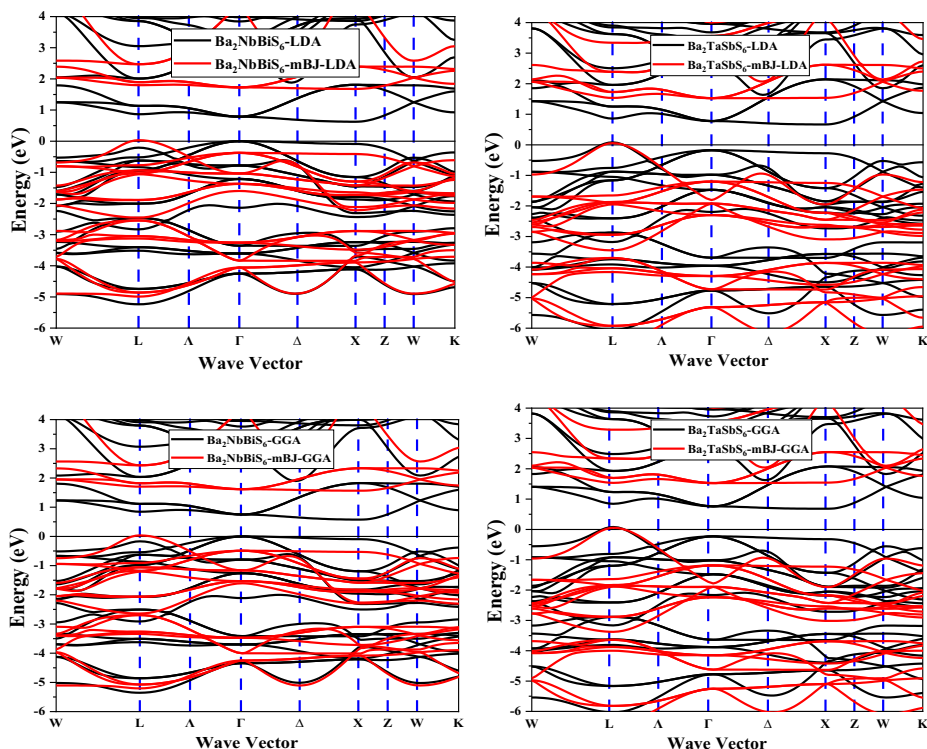

Fig. 4.   (Color online) The band structure of the Ba_2NbBiS_6 and Ba_2TaSbS_6 compounds calculated by LDA, mBJ–LDA, GGA and mBJ–GGA.

Table 3. The energy gap E_g (eV) calculated in the LDA, GGA, mBJ–GGA and mBJ–LDA approximations for the quaternary compounds of the double chalcogenide perovskites Ba_2NbBiS_6 and Ba_2TaSbS_6.

The compounds	Our calculations				Experimental results
	GGA	LDA	E_g mBJ–LDA	mBJ–GGA	
Ba_2NbBiS_6	0.628 eV	0.578 eV	1.566 eV	1.680 eV 1.690 eV[10]	GaAs: 1.42 eV $CH_3NH_3PbI_3$: 1.50 eV[11]
Ba_2TaSbS_6	0.683 eV	0.668 eV	1.527 eV	1.529 eV 1.260 eV[10]	

approximations. As schematically illustrated in Fig. 4, the band structures of Ba_2NbBiS_6 and Ba_2TaSbS_6 are semiconductor-like. High symmetry points L and X are defined as the locations of the VBM and CBM, respectively. Fermi's energy is close to the VBM. When the compounds Ba_2NbBiS_6 and Ba_2TaSbS_6 are approximated using LDA, GGA, mBJ–LDA, and mBJ–GGA, it is abundantly evident that the $Fm\bar{3}m$ phase is an indirect band deviation L → X. In addition, Table 3 provides a summary of the gap energies. At the Γ point, $BaZrS_3$ exhibits a direct bandgap, with the CBM and VBM situated therein. Ba_2SbTaS_6 $(P2_1/n)$ possesses an indirect bandgap, denoted by $\Delta E_g = 0.26$ eV, and the CBM/VBM are situated at the U point and the Γ–Y line of high symmetry, respectively. Ba_2SbTaS_6 $(R\bar{3})$ demonstrates an indirect bandgap, as indicated by its ΔE_g of 0.08 eV.[45] The CBM and VBM are situated at the L and X sites, respectively. In the case of phase $Fm\bar{3}m$, the mBJ–GGA approximation reveals a substantial and indirect fundamental gap E_g of approximately 1.680 eV and 1.529 eV for the compounds Ba_2NbBiS_6 and Ba_2TaSbS_6, respectively. The findings of our study align with the theoretical predictions and computations presented in Ref. 45.

Figure 5 illustrates the state density of the $Fm\bar{3}m$ phase for the semiconductors Ba_2NbBiS_6 and Ba_2TaSbS_6, employing the mBJ–LDA, and mBJ–GGA approximations. By converting the transitional metal element Zr(IV) ions into elements from the solitary pair s [M(III) = Bi^{+3} or Sb^{+3}] and elements from the VB group [M(V) = Nb^{+5}, Ta^{+5}], it was possible to create a class of double perovskites known as A2M(III)M(V)X6 [A = Ba; X = S]. Moreover, the VBM mostly consists of the antibonding state between the ns-M(III) and the $3p$−X anion. On the other hand, the CBM is a combination of the np-M(III) state, the $3p$-X anion, and the nd-M(V) state with the $3p$-X anion. This results in about equal masses of holes and electrons, leading to a symmetrical distribution.

A VBM state is formed when the $5s$ lone pair of Sb and the $3p$ orbital of S couple in an antiliant way, as shown by the partial density of states for Ba_2SbTaS_6. This behavior is analogous to the situation observed in $CH_3NH_3PbI_3$, where the VBM is formed by the antiliant state of Pb's s lone pair and the I–p orbital. In the case of $BaZrS_3$, the VBM primarily originates from the localized p orbital of the anion. This

behavior is analogous to that observed in conventional semiconductors like GaAs and $CuInSe_2$. The small amount of effective hole mass in $CH_3NH_3PbI_3$ is due to a single pair s adding to the antiliant VBM level. Authors in Ref. 45 explain the ambipolar conductivity phenomenon. In the case of Ba_2NbBiS_6 and Ba_2TaSbS_6, we detect a comparable electron structure, particularly about the upper dispersive valence band. A strong s–p coupling is the main factor influencing this band, which causes a decrease in effective hole mass. The effective electron mass of Ba_2SbTaS_6 is

(a)
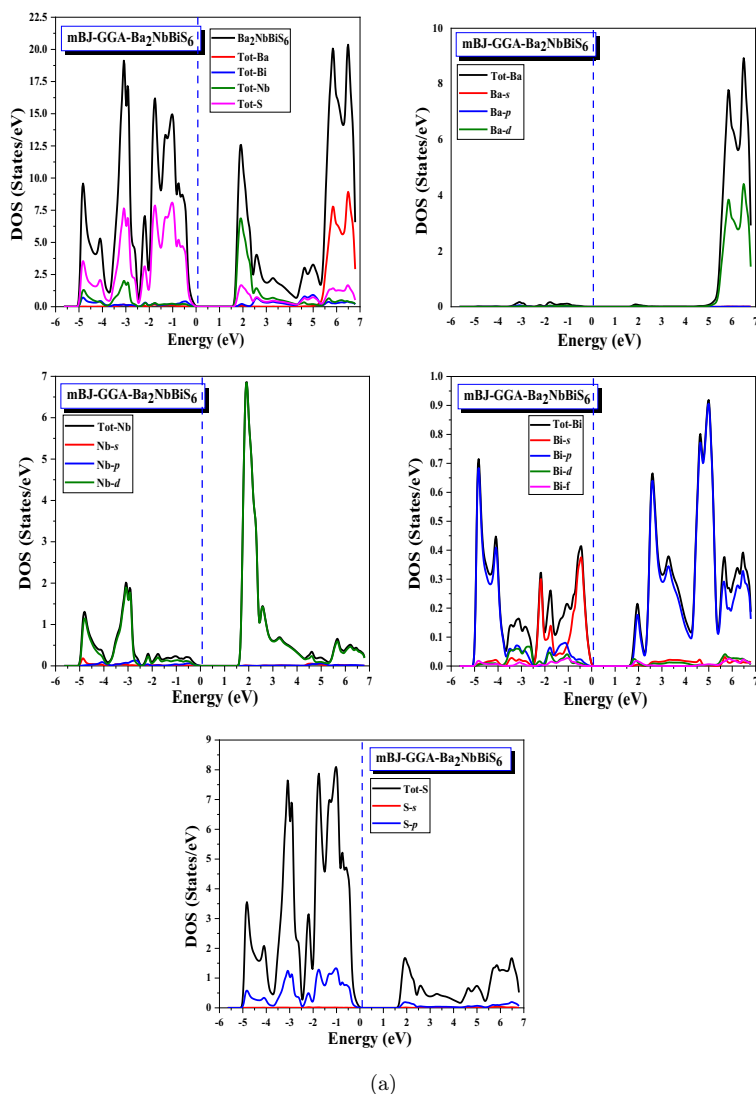
Fig. 5. (Color online) The total and partial densities of states of the (a) Ba_2NbBiS_6 and (b) Ba_2TaSbS_6 compounds were calculated by mBJ–GGA.
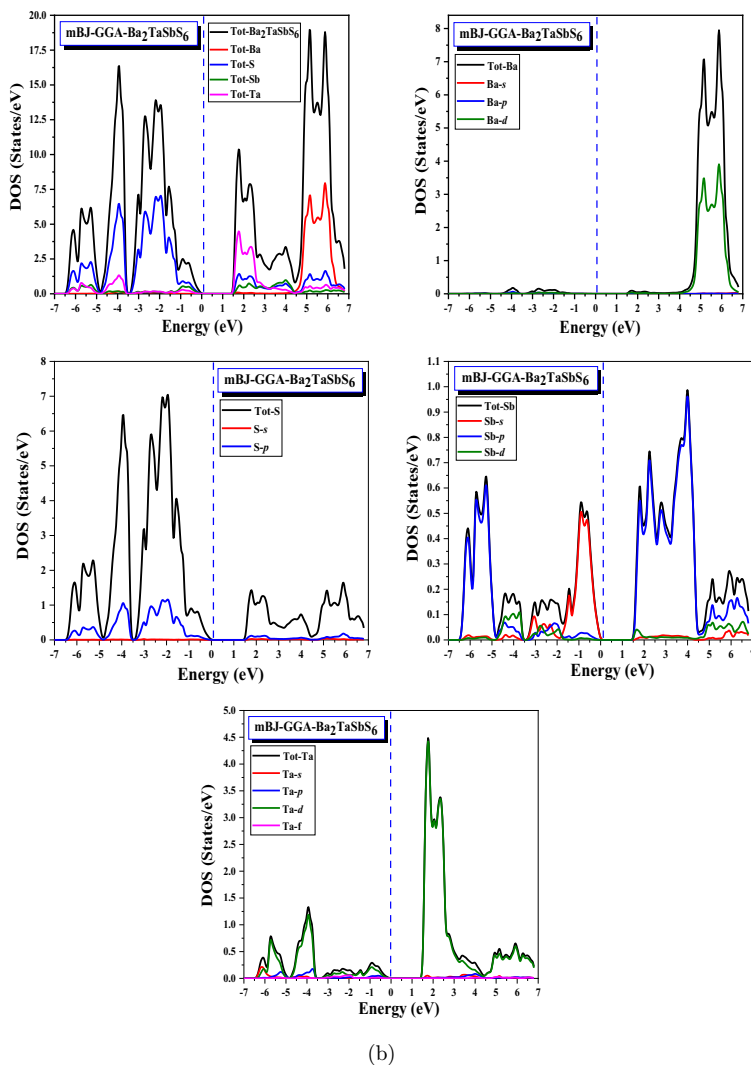
(b)

Fig. 5. (*Continued*)

much lower than that of $BaZrS_3$. This is mostly because it has a repositioned p orbital from antimony (Sb) at the CBM energy level. The existence of an indirect bandgap is often considered a drawback in the pursuit of an optimal photovoltaic cell, as it leads to a notable reduction in wavelength absorption at the band's edge. Nevertheless, an indirect band that possesses a small energy gap (ΔE_g) might promote the separation of electrons and holes, hence mitigating rapid recombination. This characteristic proves advantageous for the overall performance of the cell. The energy bandgap (ΔE_g) of chalcogenide double perovskites is estimated to be around

0.2–0.5 eV, which is comparatively lower than that of Cs_2AgBiX_6 (X = Cl, Br, I) double halogenide perovskites with a range of 0.45–0.71 eV.[45] Generally, $P2_1/n$ phases exhibit greater energy bandgaps ($\Delta E_g = 0.2$–0.5 eV) compared to $R\bar{3}$ phases. From this perspective, it may be argued that the $R\bar{3}$ phase exhibits greater suitability for photovoltaic applications compared to the $P2_1/n$ phase. Even though they have an indirect bandgap, some double perovskite chalcogenides have very small differences (<0.2 eV) between their indirect and direct bandgaps, mainly in the $R\bar{3}$ phase. Consequently, these materials can be regarded as quasi-direct bandgap semiconductors.

3.3. *Optical properties*

The bandgap value and the interaction of light energy with materials are crucial elements in determining their optical characteristics and uses. For solar cells, it is essential to achieve the highest possible absorption of light energy in the visible area, while minimizing any losses in optics. To this end, certain quantities have been calculated, such as the complex dielectric function[46] given by $\varepsilon(\omega) = \varepsilon_1(\omega) + i\varepsilon_2(\omega)$. The real component of the complex dielectric constant, $\varepsilon_1(\omega)$, measures the dispersion and polarization of light. On the other hand, the imaginary component, $\varepsilon_2(\omega)$, indicates the absorption of light and the rate at which it decays while propagating through materials.

Figure 6 displays the dependence of the imaginary component $\varepsilon_2(\omega)$ of the dielectric function on the range of photon energy spanning from 0 eV to 55 eV. The investigated quaternary compounds, namely, Ba_2NbBiS_6 and Ba_2TaSbS_6, were subjected to analysis utilizing four different approximations: LDA, GGA, mBJ–LDA and mBJ–GGA. The presented curve illustrates the material's absorption characteristics, enabling the identification of distinct transitions between bands. The spectra show that the behavior is very similar across all compounds, with the first critical points of the dielectric function beginning at 0.4152, 0.5131, 1.4876, and 1.3421 eV for Ba_2NbBiS_6 (Ba_2TaSbS_6) using the LDA, GGA, mBJ–LDA and mBJ–GGA approximations, respectively. The genesis of these points can be attributed to the optical transition occurring between the uppermost valence band and the lowermost conduction band. The threshold readings are associated with the (L $\rightarrow$ X) transition in the compounds Ba_2NbBiS_6 and Ba_2TaSbS_6, respectively. Thus, next to the fundamental peak, we notice that the main peaks reflecting the maximum absorption are located at 1.7279, 1.7279, 3.0068 and 2.9796 eV (2.4626, 2.4354, 3.7959 and 3.7687 eV) for Ba_2NbBiS_6 (Ba_2TaSbS_6) using the LDA, GGA, mBJ–LDA and mBJ–GGA approximations, respectively. Hence, it can be observed that the imaginary component of the dielectric function has a prominent peak within the visible spectrum for all materials. Following the peak, the imaginary component of the dielectric function exhibits a significant reduction as photon energy increases across every compound. The absorption bands have a broad spectrum of optical uses, ranging from the infrared to the ultraviolet (UV) regions. The lowest intensity peak is observed for the compound $Ba_2NbBiS_6 \varepsilon_2(Ba_2NbBiS_6) < \varepsilon_2(Ba_2TaSbS_6)$.
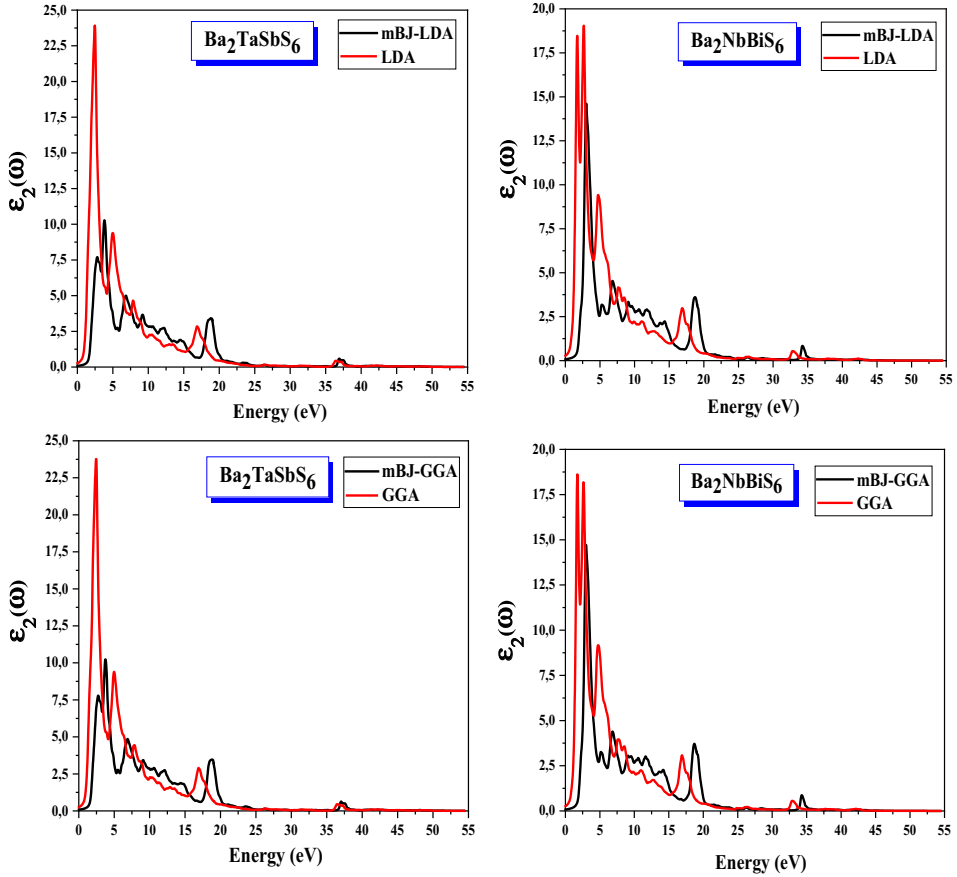
Fig. 6.   (Color online) Variation of the imaginary part of the dielectric function as a function of photon energy for the compounds Ba_2NbBiS_6 and Ba_2TaSbS_6 with the GGA, mBJ–GGA, LDA and mBJ–LDA approximations.

The extinction coefficient $k(\omega)$ quantifies the reduction or suppression of the oscillation amplitude of the incident electric field. It also measures the amount of energy absorbed by the material. Figure 7 illustrates the variation of the extinction coefficient $k(\omega)$ concerning energy for the compounds under investigation. The extinction coefficients display analogous variations for both compounds, reflecting the pattern of the imaginary component of the dielectric constant. Moreover, these variations transpire within the identical energy spectrum, as illustrated in Fig. 7. The spectra of Ba_2NbBiS_6 (Ba_2TaSbS_6) were analyzed using the LDA, GGA, mBJ–LDA and mBJ–GGA approximations. At energies of 2.7619, 2.7619, 3.3606, and 3.3606 eV (2.5714, 2.5714, 3.9864, and 3.9320 eV), the greatest possible value of the extinction coefficient was observed. This maximum value corresponds to $\varepsilon_1(0)$. After this peak, the extinction coefficient decreases rapidly with increasing photon energies for all compounds.
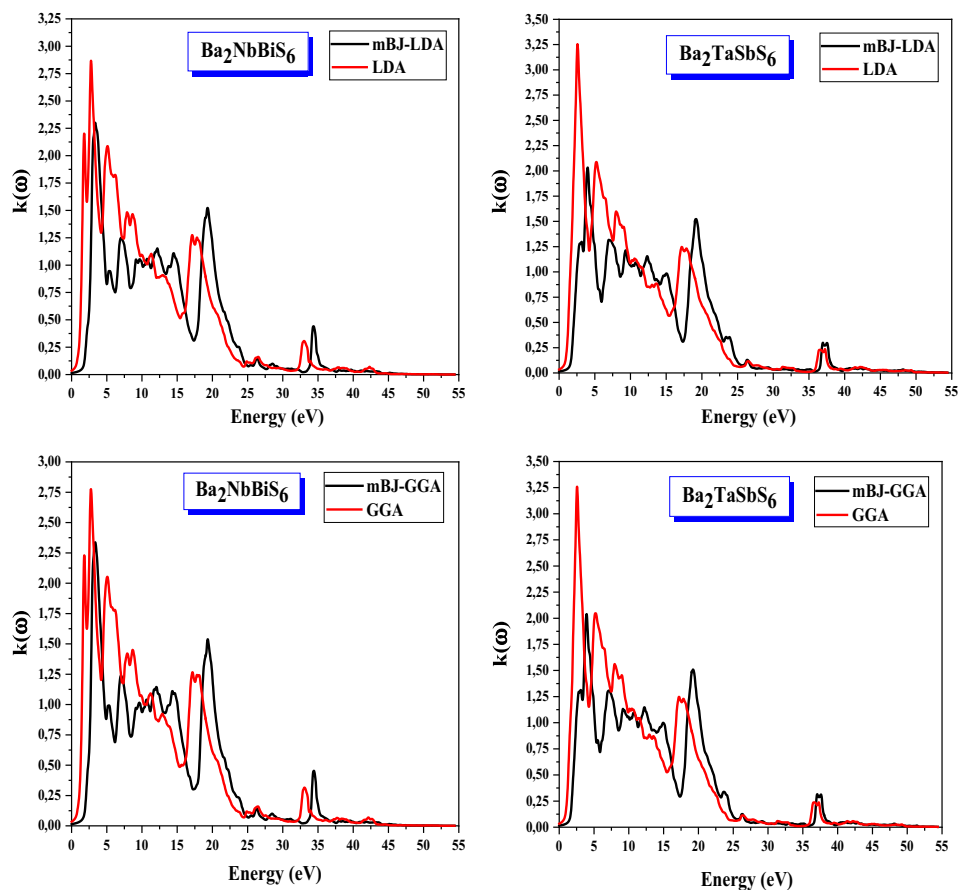
2550066-15

Fig. 7.   (Color online) Variation of the extinction coefficient as a function of photon energy for the compounds Ba_2NbBiS_6 and Ba_2TaSbS_6 with the GGA, mBJ–GGA, LDA and mBJ–LDA approximations.

Figure 8 shows the calculated results for the real $\varepsilon_1(\omega)$ (dispersive) part of the dielectric function of the compounds Ba_2NbBiS_6 and Ba_2TaSbS_6. The zero crossing of the spectra signifies the nonexistence of scattering. The peak visible at around $0\,eV$ in the dielectric function represents the material's sensitivity to an external electric field at static or low frequencies. This peak, also known as the static or high-frequency dielectric constant, represents the material's ability to store an electric charge at zero frequency or for a long period of time. It is often linked to the polarization of the material, which occurs when charges move in reaction to an electric field. The real component of the values $\varepsilon_1(0)$ exhibits a rising trend as the photon energy increases. It reaches prominent peaks before eventually reaching a value of zero. After traversing a minimal point, the dispersive component returns to zero. The main peaks $\varepsilon_1(\omega)$ obtained from the calculations are located at 1.4286, 2.7075, 1.4830, and $2.7075\,eV$ (1.3741, 2.0272, 1.4013 and $2.00\,eV$) for Ba_2NbBiS_6 (Ba_2TaSbS_6) using the LDA, mBJ–LDA, GGA and mBJ–GGA approaches, respectively. According to the
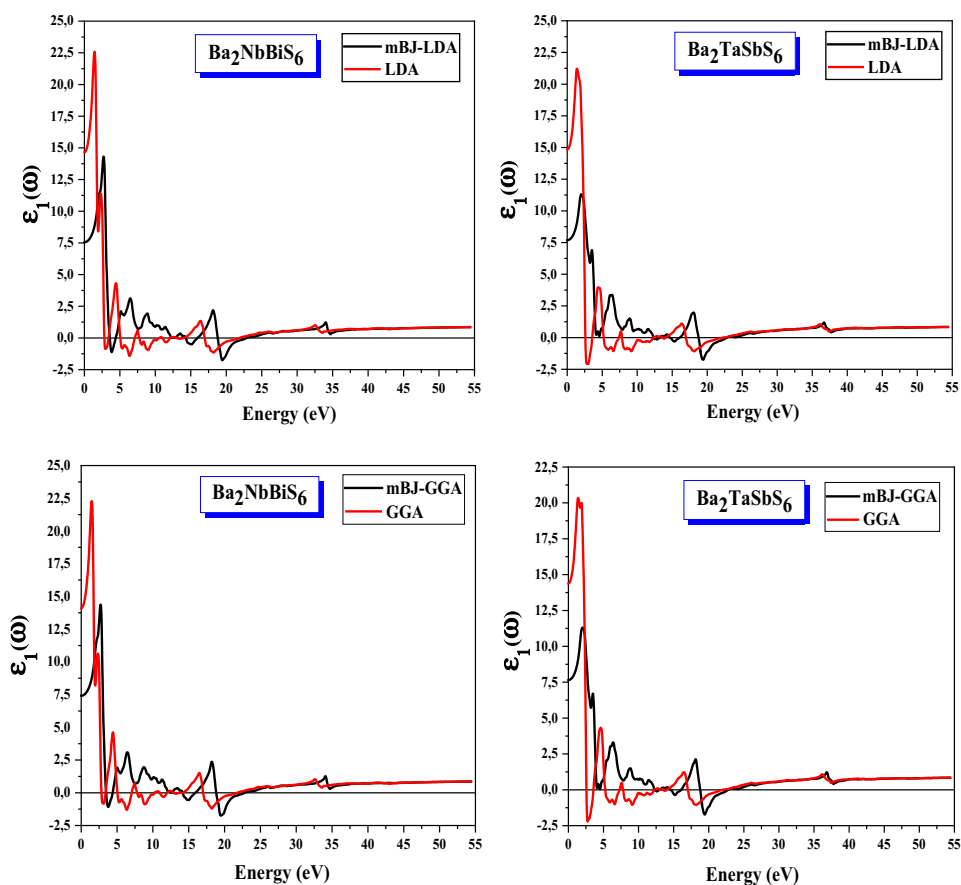
Fig. 8. (Color online) Variation of the real part of the dielectric function as a function of photon energy for the compounds Ba_2NbBiS_6 and Ba_2TaSbS_6 with the GGA, mBJ–GGA, LDA and mBJ–LDA approximations.

mBJ–LDA and mBJ–GGA approximations, these are situated in the visible spectrum. However, the LDA and GGA approximations assign the principal peak to the infrared region. At energies of 1.7279, 1.7279, 3.0068, and 2.9796 eV (2.4626, 2.4354, 3.7959, and 3.7687 eV), the real part of the dielectric function for Ba_2NbBiS_6 (Ba_2TaSbS_6) becomes zero as approximated by the LDA, GGA, mBJ–LDA and mBJ–GGA, respectively. There is a gradual decrease towards zero again observed at energy levels of approximately 21.9459, 22.9256, 21.9187, and 22.8167 eV (22.8439, 24.3405, 22.8711 and 24.3678 eV) for the compound Ba_2NbBiS_6 (Ba_2TaSbS_6) when employing the LDA, mBJ–LDA, GGA and mBJ–GGA approximations, respectively. Both materials showed resonance frequencies within the energy range of 0–20 eV, which are observed as polarization peaks exhibiting variations, as shown in Fig. 8. Following these variations, there is a notable decrease in energy at approximately 20 eV in both materials. Consequently, the waves' phase velocity transforms

2550066-17

into the group velocity, leading to an area of energy that exceeds the speed of light. The peak with the maximum intensity is noted for the compound Ba_2NbBiS_6 ($\varepsilon_1(Ba_2NbBiS_6) > \varepsilon_1(Ba_2TaSbS_6)$). Furthermore, Ba_2TaSbS_6 exhibits a higher dielectric constant than the compound Ba_2NbBiS_6 using the LDA and GGA approximations, while this trend is reversed using the mBJ–LDA and mBJ–GGA approximations, ($\varepsilon_1(0)_{(Ba_2NbBiS_6)} > \varepsilon_1(0)_{(Ba_2TaSbS_6)}$). Penn explained this effect in the following equation $\varepsilon_1(0) \approx 1 + (\frac{\hbar\omega_P}{E_g})^2$,[47] where E_g and ω_P represent the energy bandgap and plasma frequency, respectively. This implies that a narrow energy gap, denoted as E_g, results in a significant value of $\varepsilon_1(0)$. The calculation and summarization $\varepsilon_1(0)$ can be seen in Table 4.

The refractive index, denoted as $n(\omega)$, is a parameter that quantifies the extent of light reflection upon reaching an interface. The observation of light energy dispersion and material transparency can be derived from the computed values of their refractive indices $n(\omega)$. The significance of these optical qualities is enhanced in numerous applications. The static refractive index is nonzero because of the interaction between photons and electrons in the medium. Due to this interaction, photons undergo a deceleration when traversing the investigated compounds, resulting in refractive indices that surpass 1. Fluctuations in the refractive index values are found for both substances within the energy range of 0–55 eV. Both compounds display optically anisotropic properties for incident photons of both low and high energy, as indicated by the observed behavior. The spectra are depicted in Fig. 9, wherein the refractive index generally conforms to the profile of the associated real component, as governed by the following relationship: $n(0) = \sqrt{\varepsilon_1(0)}$. It can be seen in the refractive index spectra that excitonic transitions cause clear peaks to appear at the edge of the energy bandgap. The refractive indices at zero frequency for Ba_2NbBiS_6 and Ba_2TaSbS_6, using the GGA, mBJ–GGA, LDA and mBJ–LDA approximations, are as follows: $n(0) = 3.7562, 2.7227, 3.8280, 2.7488$ ($n(0) = 3.7930, 2.6810, 3.8533, 2.6851$), respectively. The refractive index demonstrates an upward trend as the frequency increases until it reaches around 2 eV. Beyond this point, it undergoes a decline until approximately 21 eV, displaying nonlinear characteristics. The static refractive index that has been determined is presented in the same table alongside other relevant information. As far as current knowledge is concerned, there is a lack of experimental or theoretical evidence that may be used for comparative analysis.

The variation in reflectivity $R(\omega)$ is shown in Fig. 10 as a function of energy for the compounds Ba_2NbBiS_6 and Ba_2TaSbS_6 using the GGA, mBJ–GGA, LDA, and

Table 4. $\varepsilon_1(0)$ and $n(0)$ calculated for the compounds Ba_2NbBiS_6 and Ba_2TaSbS_6 with the LDA, GGA, mBJ–GGA and mBJ–LDA approximations.

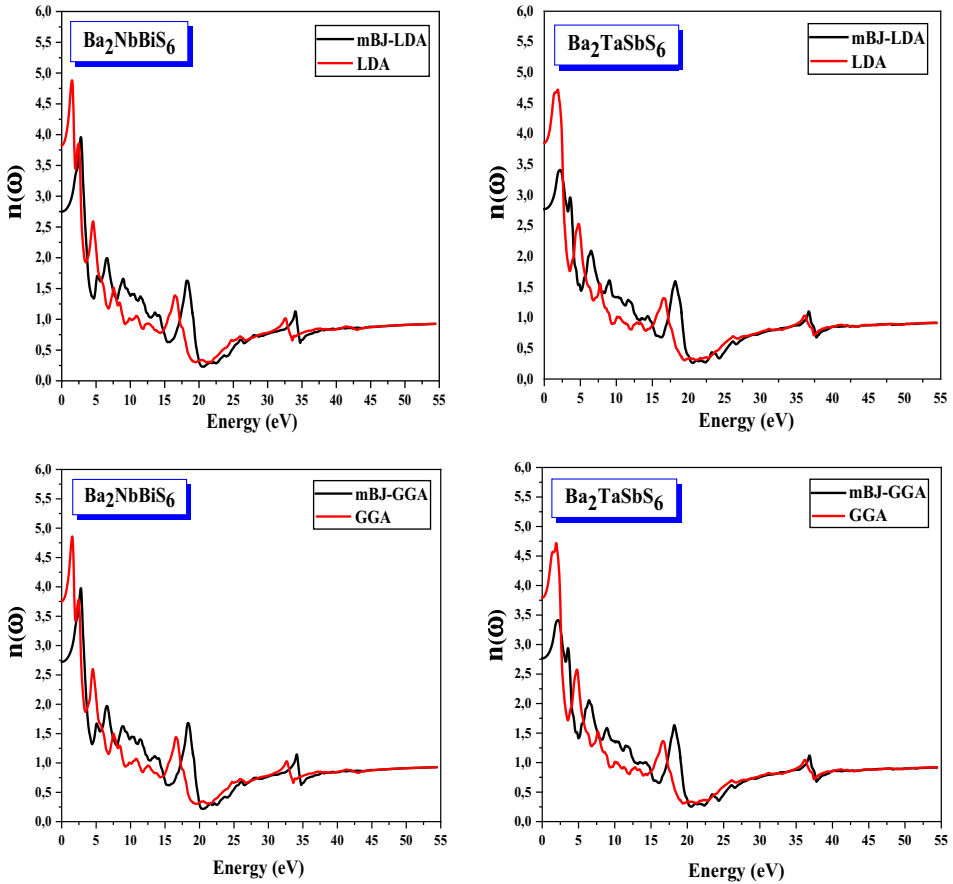| The compounds		$\varepsilon_1(0)$				$n(0)$			
		GGA	mBJ–GGA	LDA	mBJ–LDA	GGA	mBJ–GGA	LDA	mBJ–LDA
Ba_2NbBiS_6	ε_1	1.410	7.413	1.465	7.556	n	3.756	2.722	3.828	2.748
Ba_2TaSbS_6	ε_1	1.438	7.187	1.484	7.209	n	3.793	2.681	3.853	2.685

Fig. 9.   (Color online) Variation of refractive index as a function of photon energy for the compounds Ba_2NbBiS_6 and Ba_2TaSbS_6 with the GGA, mBJ–GGA, LDA and mBJ–LDA approximations.

mBJ–LDA approximations. Based on the provided data, it can be noticed that the quaternary compounds Ba_2NbBiS_6 and Ba_2TaSbS_6 exhibit low reflectivity at low energies. For example, the reflectivity values for Ba_2NbBiS_6 are 34.31% using the LDA method, 21.76% using the mBJ–LDA method, 33.58% using the GGA method, and 21.41% using the mBJ–GGA method. Similarly, for Ba_2TaSbS_6, the reflectivity values are measured as 34.56%, 22.07%, 33.96%, and 21.99%, respectively, utilizing the aforementioned approximations. The reflectance throughout the energy range that corresponds to the bandgap of both compounds is significantly low, suggesting that the materials allow incident photons to pass through them without obstruction. The high level of transparency exhibited by these compounds in the low energy region indicates their potential for use in lens manufacturing, making them a highly intriguing option for such applications. At low energies, reflectivity increases with increasing photon energy to reach a secondary (main) peak, then increases again to reach a main (secondary) peak with the mBJ–LDA and mBJ–GGA approximations
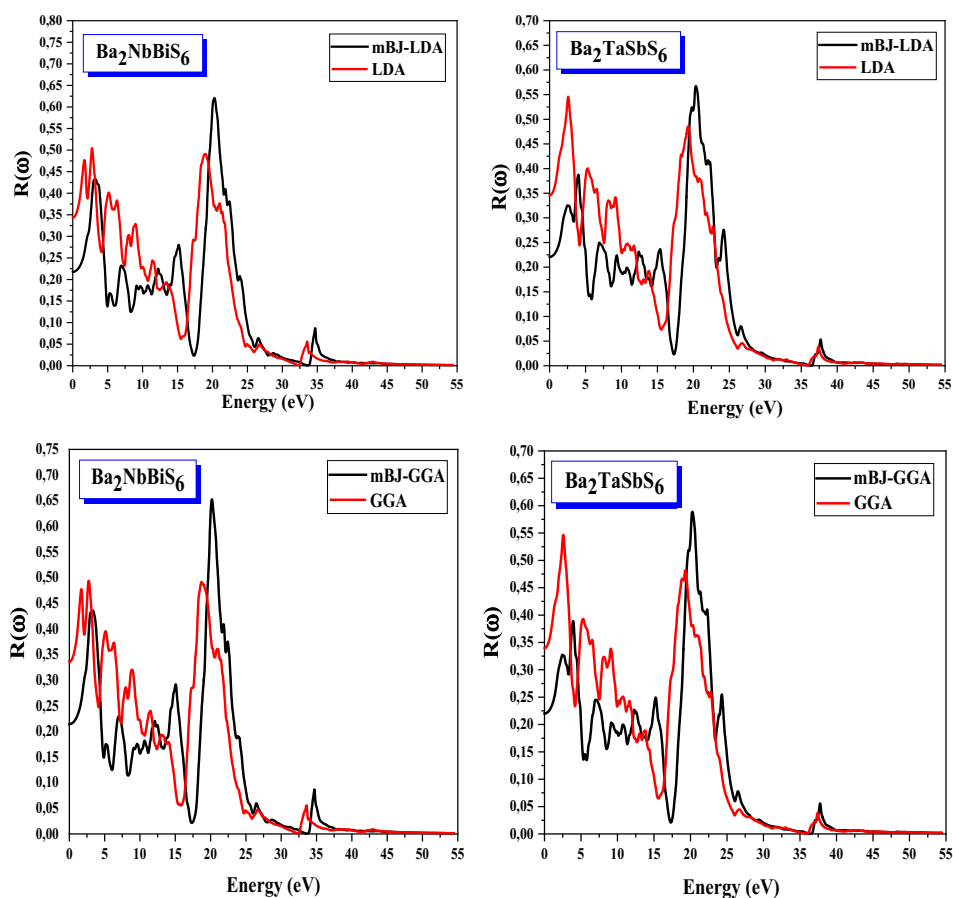
Fig. 10. (Color online) Variation of reflectivity as a function of photon energy for the compounds Ba_2NbBiS_6 and Ba_2TaSbS_6 with the GGA, mBJ–GGA, LDA and mBJ–LDA approximations.

(LDA and GGA). The main peak occurs at energies of 2.7619, 20.2861, 2.7347, and 20.1772 eV (2.5714, 20.2861, 2.5714 and 20.2588 eV) for the compounds Ba_2NbBiS_6 (Ba_2TaSbS_6) using the LDA, mBJ–LDA, GGA and mBJ–GGA approaches, respectively. The reflectivity of the quaternary compound Ba_2NbBiS_6 is higher than that of the quaternary compound Ba_2TaSbS_6.

The absorption coefficients $I(\omega)$ of the quaternary compounds of the double chalcogenide perovskites Ba_2NbBiS_6 and Ba_2TaSbS_6 with the LDA, mBJ–LDA, GGA, and mBJ–GGA approximations are shown in Fig. 11. From this figure, there is a considerable increase in the absorption coefficient, which is present in the low energies. It should be noted that at the highest energies, this increase reaches its maximum value, then decreases to reach a secondary peak in the far UV region. The compounds Ba_2NbBiS_6 and Ba_2TaSbS_6 exhibit efficient absorption of electromagnetic radiation at energy thresholds of 1.566 eV and 1.527 eV, respectively, when
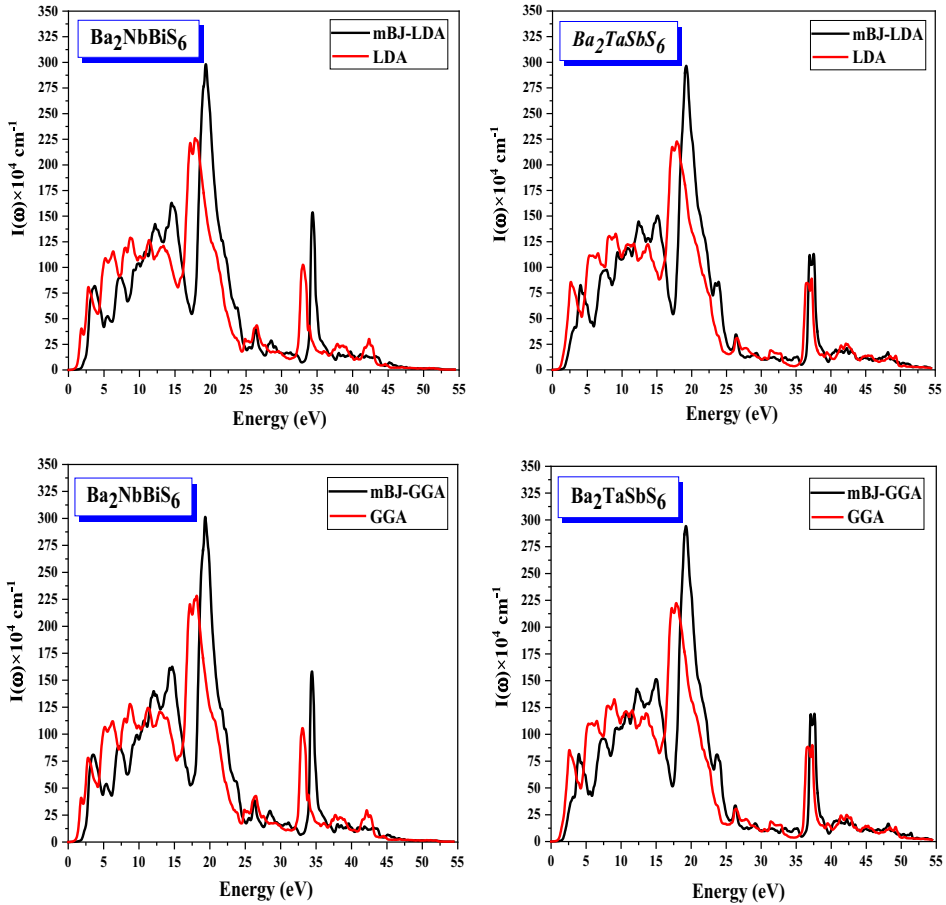
Fig. 11. (Color online) Variation of the absorption coefficient as a function of photon energy for the compounds Ba_2NbBiS_6 and Ba_2TaSbS_6 with the GGA, mBJ–GGA, LDA and mBJ–LDA approximations.

using mBJ–LDA. These energy thresholds are within the suitable range of 1.3–1.7 eV for photovoltaic applications in bulk materials. Remarkably, these threshold points precisely align with the bandgap regions of both materials. Materials have low absorption coefficients at energies below the bandgap because the photons do not have enough energy to excite electrons across the bandgap. However, once the energy of the incoming photons reaches or exceeds the energy of the bandgap, the absorption coefficient undergoes a significant increase. The strong peak is observed at energies of 17.8370, 19.3337, 18.1363, and 19.3609 eV (17.8914, 19.2248, 17.8914 and 19.2520 eV) for the compounds Ba_2NbBiS_6 (Ba_2TaSbS_6) using the LDA, mBJ–LDA, GGA and mBJ–GGA approximations, respectively. The absorption spectra show maxima in the energy range 5.0205–22.0548 eV (8.0137–21.89 eV) for the compound Ba_2NbBiS_6 (Ba_2TaSbS_6) using the LDA and mBJ–LDA approximations. The maximum absorption is attributed to the compound Ba_2NbBiS_6. The identification

of peak levels of absorption in the near-UV spectrum suggests that the compounds under investigation demonstrate absorption characteristics within this wavelength range. Consequently, these materials possess great potential as suitable options for UV photo-detectors, UV light emitters, and power electronic applications. This is primarily owing to their inherent absorption limits and the presence of the most intense absorption peaks. The comprehensive examination of optical properties reveals exceptional photoelectric features, suggesting significant potential for implementation in the absorber part of photovoltaic cells. The absorption coefficient is $(10^4–10^5 \, \text{cm}^{-1})$ for the solar cell application. In our case the absorption coefficient is 30.14×10^5, and $29.43 \times 10^5 \, \text{cm}^{-1}$ for Ba_2NbBiS_6 and Ba_2TaSbS_6, respectively according to the mBJ–GGA. With such outstanding optical properties, it exhibits high absorption intensity. Therefore, it can be effectively utilized as a key candidate material for scaled optoelectronic and photovoltaic devices.
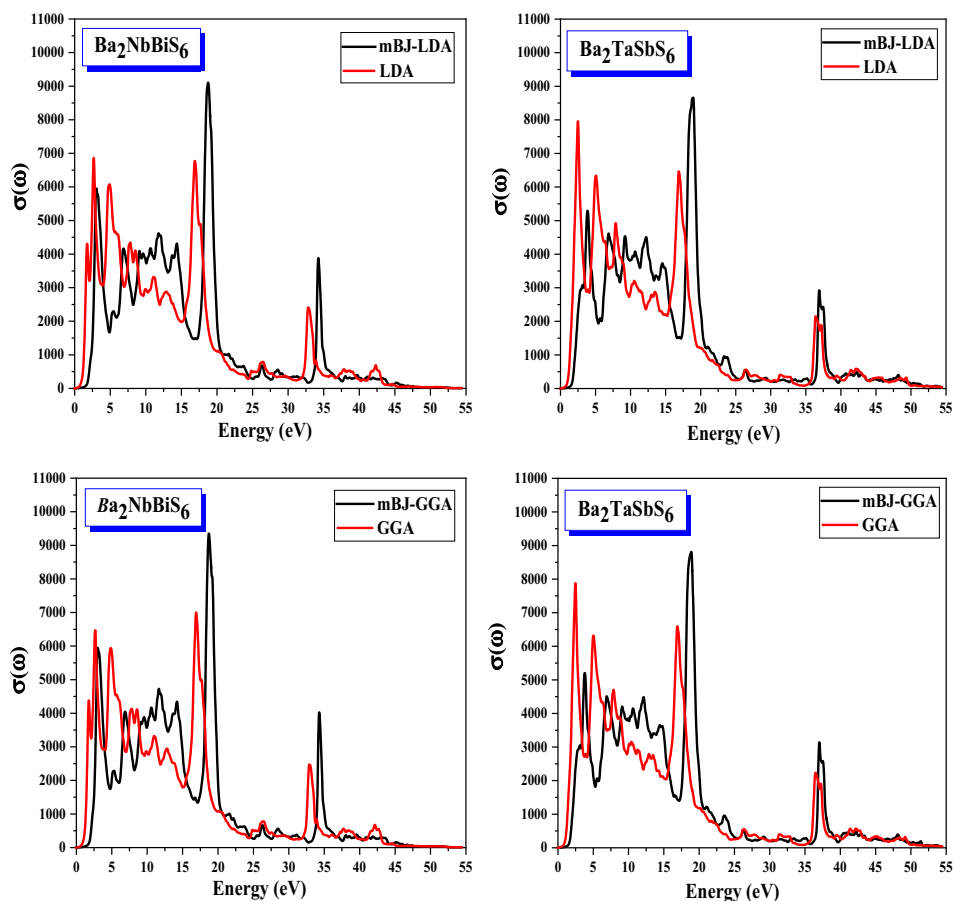

Fig. 12.   (Color online) Variation of optical conductivity as a function of photon energy for the compounds Ba_2NbBiS_6 and Ba_2TaSbS_6 with the GGA, mBJ–GGA, LDA and mBJ–LDA approximations.

The optical conductivity, denoted as $\sigma(\omega)$, describes the conduction of electrons that is caused by an externally applied electromagnetic field. The optical conductivity spectra $\sigma(\omega)$ of the quaternary compounds of the double chalcogenide perovskites Ba_2NbBiS_6 and Ba_2TaSbS_6 with the LDA, mBJ–LDA, GGA and mBJ–GGA approximations are shown in Fig. 12. The optical conductivity spectrum exhibits many peaks that correspond to transitions between bands. Based on Fig. 12, it is clear that the optical conductivity of both compounds starts at a similar energy level as the energy bandgap. The measured optical conductivity threshold in both compounds validates the anticipated energy of the bandgap. Moreover, it is apparent from the image that the optical conductivity curves for both compounds have identical patterns. Ba_2NbBiS_6 exhibits greater optical conductivity compared to Ba_2TaSbS_6.
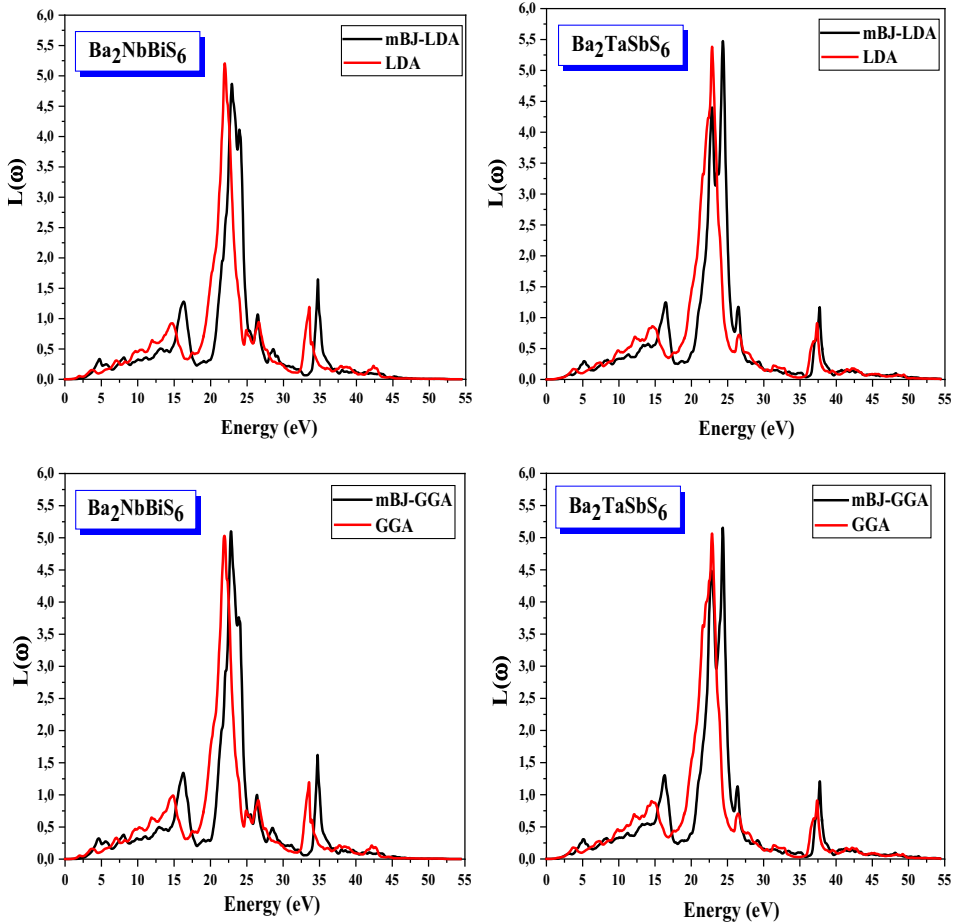

Fig. 13. (Color online) Variation of the ELF as a function of photon energy for the compounds Ba_2NbBiS_6 and Ba_2TaSbS_6 with the GGA, mBJ–GGA, LDA and mBJ–LDA approximations.

The electron energy-loss function (ELF) can be used to characterize the relationships between intra-band, inter-band, and Plasmon interactions. The ELF measures the amount of energy that is released by a fast-moving electron as it passes through a substance. The ELF $L(\omega)$ can be determined using the dielectric function, as previously stated in our earlier publications.[48–57] Figure 13 illustrates the energy loss spectra $L(\omega)$, which exhibit notable magnitudes within the energy range of 20.4221–24.5855 eV (20.9119 eV and 25.0208 eV) for Ba_2NbBiS_6 (Ba_2TaSbS_6) when employing the LDA and mBJ–LDA approximations. The intense peak is observed at an energy of 21.9459, 22.9256, 21.9187, and 22.8167 eV (22.8439, 24.3405, 22.8711 and 24.3678 eV) for Ba_2NbBiS_6 (Ba_2TaSbS_6) using the LDA, mBJ–LDA, GGA and mBJ–GGA approximations, respectively. The highest energy loss peak is attributed to the Ba_2TaSbS_6 compound. The plasma frequency ω_p of its peak position is 3.3341×10^{16}, 3.4830×10^{16}, 3.3300×10^{16} and $3.4664 \times 10^{16}\,s^{-1}$ (3.4705×10^{16}, 3.6979×10^{16}, 3.4747×10^{16} and $3.7021 \times 10^{16}\,s^{-1}$) for Ba_2NbBiS_6 (Ba_2TaSbS_6) using the LDA, mBJ–LDA, GGA and mBJ–GGA approximations, respectively. From the examination of the optical properties, it can be deduced that these compounds display notable absorption and optical conduction in the high-energy regions. The finding indicates that these compounds are highly suitable for applications using high-frequency UV devices.

4. Conclusion

The study employs first-principles methods to investigate the structural, electronic, and optical properties of Ba_2NbBiS_6 and Ba_2TaSbS_6 chalcogenide-based double perovskites. Both compounds exhibit a perovskite structure with specific bond lengths determined by different approximations. Despite a lack of experimental data, the research provides valuable energy values and compressibility modulus insights. Furthermore, it can be observed that the compressibility modulus of the compound Ba_2TaSbS_6 is higher than that of the compound Ba_2NbBiS_6, regardless of the approximation used. The band structure analysis reveals a semiconducting nature for both compounds, with a large and indirect fundamental gap. The study emphasizes the importance of indirect bandgaps with small ΔE_g for optimal solar cell performance. Optical parameters and absorption characteristics indicate that these compounds may be promising for UV photodetectors, UV light emitters, and power electronics applications. In this study, chemical mutation techniques are employed to customize the characteristics of double-sulfide, to develop durable, lead-free perovskite materials suitable for use in solar devices.

Acknowledgments

ORCID

H. Baaziz ⬡ https://orcid.org/0000-0003-4860-2740

T. Ghellab ⬡ https://orcid.org/0009-0001-6823-4335

Z. Charifi ⬡ https://orcid.org/0000-0003-3875-4716

References

1. NREL, (2018), https://www.nrel.gov/pv/assets/pdfs/pv-efficiencies-07-17-2018.pdf.
2. A. Kojima *et al.*, *J. Am. Chem. Soc.* **131**, 6050 (2009).
3. M. Kulbak, D. Cahen and G. Hodes, *J. Phys. Chem. Lett.* **6**, 2452 (2015).
4. J. Liang *et al.*, *J. Am. Chem. Soc.* **138**, 15829 (2016).
5. P. Luo *et al.*, *J. Phys. Chem. Lett.* **7**, 3603 (2016).
6. A. Swarnkar *et al.*, *Science* **354**, 92 (2016).
7. P. Wang *et al.*, *Nat. Commun.* **9**, 2225 (2018).
8. Y. Wang *et al.*, *J. Am. Chem. Soc.* **140**, 12345 (2018).
9. C. Liu *et al.*, *J. Am. Chem. Soc.* **140**, 3825 (2018).
10. D. Bai *et al.*, *ACS Energy Lett.* **3**, 970 (2018).
11. H. Bian *et al.*, *Joule* **2**, 1 (2018).
12. W. Shockley and H. J. Queisser, *J. Appl. Phys.* **32**, 510 (1961).
13. E. T. McClure *et al.*, *Chem. Mater.* **28**, 1348 (2016).
14. A. H. Slavney *et al.*, *J. Am. Chem. Soc.* **138**, 2138 (2016).
15. G. Volonakis *et al.*, *J. Phys. Chem. Lett.* **7**, 1254 (2016).
16. T. T. Tran *et al.*, *Mater. Horiz.* **4**, 688 (2017).
17. W. Deng *et al.*, *Appl. Phys. Lett.* **111**, 151602 (2017).
18. M. R. Filip *et al.*, *J. Phys. Chem. Lett.* **7**, 2579 (2016).
19. C. N. Savory, A. Walsh and D. O. Scanlon, *ACS Energy Lett.* **1**, 949 (2016).
20. G. Volonakis *et al.*, *J. Phys. Chem. Lett.* **8**, 772 (2017).
21. W. Meng *et al.*, *J. Phys. Chem. Lett.* **8**, 2999 (2017).
22. X.-G. Zhao *et al.*, *J. Am. Chem. Soc.* **139**, 2630 (2017).
23. Z. Xiao *et al.*, *J. Am. Chem. Soc.* **139**, 6054 (2017).
24. Y.-Y. Sun *et al.*, *Nano Lett.* **15**, 581 (2015).
25. W. Meng *et al.*, *Chem. Mater.* **28**, 821 (2016).
26. S. Perera *et al.*, *Nano Energy* **22**, 129 (2016).
27. S. Niu *et al.*, *Adv. Mater.* **29**, 1604733 (2017).
28. M. G. Ju *et al.*, *Adv. Energy Mater.* **7**, 1700216 (2017).
29. J. P. Perdew, K. Burke and M. Ernzerhof, *Phys. Rev. Lett.* **77**, 3865 (1996).
30. P. Blaha *et al.*, WIEN2k an augmented plane wave + local orbitals program for calculating crystal properties, revised edition, WIEN2k 19.1 (2019).
31. J. P. Perdew and Y. Wang, *Phys. Rev. B* **45**, 13244 (1992).
32. F. D. Murnaghan, *Proc. Nat. Acad. Sci. USA* **30**, 244 (1944).
33. F. Tran and P. Blaha, *Phys. Rev. Lett.* **102**, 226401 (2009).
34. N. Rahman *et al.*, *Optik* **299**, 171590 (2024), doi: 10.1016/j.ijleo.2023.171590.
35. J. Saddique *et al.*, *Mater. Sci. Semicond. Process.* **139**, 106345 (2022), doi: 10.1016/j.mssp.2021.106345.
36. F. T. Tahir *et al.*, *RSC Adv.* **13**, 18788 (2023), doi: 10.1039/D3RA02878J.
37. A. Jehan *et al.*, *Optik* **287**, 171088 (2023), doi: 10.1016/j.ijleo.2023.171088.
38. S. A. Khattak *et al.*, *CS Omega* **8**, 5274 (2023), doi: 10.1021/acsomega.2c05845.
39. A. Jehan *et al.*, *Opt. Quantum Electron.* **56**, 169 (2024), doi: 10.1007/s11082-023-05750-4.

40. N. Rahman *et al.*, *Eur. Phys. J. Plus* **136**, 347 (2021), doi: 10.1140/epjp/s13360-021-01177-6.
41. M. Husain *et al.*, *Int. J. Energy Res.* **46**, 2446 (2022), doi: 10.1002/er.7319.
42. M. Arif *et al.*, *Int. J. Energy Res.* **46**, 2467 (2022), doi: 10.1002/er.7321.
43. V. M. Goldschmidt, *Naturwissenschaften* **14**, 477 (1926).
44. S. Vasala and M. Karppinen, *Prog. Solid State Chem.* **43**, 1 (2015).
45. Q. Sun, H. Chen and W.-J. Yin, *Chem. Mater.* **31**, 244 (2019).
46. N. V. Smith, *Phys. Rev. B* **3**, 1862 (1971).
47. D. R. Penn, *Phys. Rev. B* **128**, 2093 (1962).
48. T. Ghellab *et al.*, *Mater. Res. Express* **6**, 075906 (2019).
49. H. Mekki *et al.*, *Solid State Commun.* **363**, 115103 (2023), doi: 10.1016/j.ssc.2023.115103.
50. T. Ghellab *et al.*, *Int. J. Energy Res.* **43**, 3653 (2019).
51. T. Ghellab *et al.*, *Int. J. Mod. Phys. B* **33**, 1950234 (2019).
52. I. Mili1 *et al.*, *Int. J. Mod. Phys. B* **35**, 2150100 (2021).
53. T. Ghellab *et al.*, *Physica B* **653**, 414678 (2023), doi: 10.1016/j.physb.2023.414678.
54. A. Telfah *et al.*, *J. Magn. Magn. Mater.* **562**, 169822 (2022).
55. T. Ghellab *et al.*, *Mater. Sci. Semicond. Process.* **141**, 106415 (2022).
56. Z. Charifi *et al.*, *Int. J. Energy Res.* **46**, 13855 (2022), doi: 10.1002/er.8104.
57. T. Ghellab *et al.*, *Phys. Scr.* **91**, 045804 (2016).